Rare Met. (2022) 41(6):1899–1910
https://doi.org/10.1007/s12598-021-01933-8

RARE METALS

ORIGINAL ARTICLE

Determining hydrothermal deactivation mechanisms on Cu/SAPO-34 NH_3-SCR catalysts at low- and high-reaction regions: establishing roles of different reaction sites

Qing-Jin Lin, Ming-Ming Pei, Pan Yao, Shi Xu, Shu-Hao Xu, Shuang Liu, Hai-Di Xu*, Yi Dan*, Yao-Qiang Chen

Received: 21 August 2021 / Revised: 29 October 2021 / Accepted: 11 November 2021 / Published online: 7 March 2022

Abstract Hydrothermal deactivation is a constant challenge in commercial catalytic process aimed at NO_x emission control, which may be observed in the low (150–400 °C) or high (400–550 °C)-reaction regions. To the best of our knowledge, there is a lack of systematic research regarding the correlation between the reaction sites and the mechanism of hydrothermal degradation at various reaction regions. For a targeted investigation of this, Cu/zeolite catalysts have been prepared using different amounts of polyvinyl alcohol for adjusting their redox and acid properties. These catalysts exhibit hydrothermal deactivation in different reaction regions. No change is observed in the reaction mechanism even with hydrothermal deactivation, but various reaction sites determine the performance deterioration in the low- and high-reaction regions. The redox properties and weak acid sites affect the hydrothermal deactivation in the low-reaction region, whereas the moderate/strong acid sites related to the structure mainly influence the hydrothermal deactivation in the high-reaction region. This work provides several theoretical insights for optimizing the hydrothermal stabilities of Cu/zeolite catalysts.

Keywords Deterioration mechanism; Bifunctional sites; Temperature regions; Selective catalytic reduction; Cu/zeolite

Supplementary Information The online version contains supplementary material available at https://doi.org/10.1007/s12598-021-01933-8.

Q.-J. Lin, Y. Dan*
State Key Laboratory of Polymer Materials Engineering, Polymer Research Institute, Sichuan University, Chengdu 610064, China
e-mail: danyi@scu.edu.cn

M.-M. Pei, S.-H. Xu, Y.-Q. Chen
Key Laboratory of Green Chemistry and Technology, College of Chemistry, Sichuan University, Ministry of Education, Chengdu 610064, China

P. Yao, S. Liu, H.-D. Xu*
Institute of New Energy and Low-Carbon Technology, Sichuan University, Chengdu 610064, China
e-mail: xuhaidi@scu.edu.cn

S. Xu
Weichai Power Co., Ltd, Weifang 261061, China

H.-D. Xu, Y.-Q. Chen
Sichuan Provincial Automobile Exhaust Purification Engineering Technology Research Center, Chengdu 610064, China

H.-D. Xu, Y.-Q. Chen
Sichuan Provincial Environmental Protection Environmental Catalytic Materials Engineering Technology Center, Chengdu 610064, China

1 Introduction

As the core of post-combustion removal of harmful nitrogen oxides (NO_x) produced by lean-burn engines, selective catalytic reduction with NH_3 (NH_3-SCR) catalyst is bifunctional: Acid sites adsorb/activate NH_3 molecules and redox sites promote the cycling of metal ions between high and low valence [1]. The activation of the gases at bifunctional sites occurs via two types of mechanisms: (1) the Langmuir–Hinshelwood (L–H) mechanism, where adsorbed ammonia species react with nitrites/nitrates; (2) the Eley–Rideal (E–R) mechanism, where the adsorbed ammonia species react with NO_x gas [2]. Because of the difference in the adsorption/activation of NO and NH_3 at

the reaction sites, the low-temperature (150–400 °C) reaction mainly follows the L–H mechanism, whereas the high-temperature (400–550 °C) reaction generally proceeds via the E–R mechanism [3, 4].

Commercial NH_3-SCR catalysts function under the high-temperature ($T > 650$ °C) hydrothermal ($\sim$ 10 vol% H_2O) condition [5–8], which generally accelerates performance deterioration. Hence, high-temperature hydrothermal stability is critical. Remarkably, in previous studies [9–11], we observed hydrothermal deactivation to varying degrees at low (150–400 °C) and high (400–550 °C) temperatures with "seagull"-shaped NO_x conversion profiles using the catalysts following hydrothermal aging. Sacrificed bifunctional sites may be related to this "seagull"-shaped profile [12–14]. Focusing on the hydrothermal stabilities of NH_3-SCR catalysts, deep understanding of the correlation between the determined reaction sites and the deactivation mechanism at the low (150–400 °C) and high (400–550 °C) temperatures is required. However, to the best of our knowledge, there remains a lack of systematic research regarding this correlation. Thus, these sites should be altered to modify the catalytic and deactivation properties of the catalysts to investigate this relationship.

CHA zeolites (SAPO-34 and SSZ-13) are representative supports for NO_x removal. The hydrothermal deactivation of SAPO-34 after extended storage at $T < 70$ °C is mysterious. However, Cu/SAPO-34 still displays more advantages compared with Cu/SSZ-13, such as low synthetic cost, good low-temperature activity, and excellent high-temperature hydrothermal stability. Si atoms substitute Al or P atoms in the AlPO framework, forming Si(OAl) structures. Owing to the different electronegativity of the Si and Al atoms, extra protons are required to neutralize the framework of the zeolite [15]. These protons in the Si(OAl) structures provide ion-exchange sites for anchoring copper ions and acid sites for NH_3 adsorption. Thus, modifying the Si(OAl) structures may alter the reactant sites. The silicate ions depolymerized from SiO_2 sols participate in the formation of Si(OAl) structures. The surfactant polyvinyl alcohol (PVA) adsorbs on the surfaces of the SiO_2 sols, where decreased surface energy prevents the sols from growing into large particles, affecting the formation of the Si(OAl) structures [16–18]. In addition, the hydroxyl groups of PVA react with the hydroxyls located at the surfaces, pores, and channels of AlPO [17], affecting the reaction between partial silicate ions and AlPO, which also alters the Si(OAl) structures. Herein, PVA may be the second structure-directing agent affecting the Si(OAl) structures, altering the redox and acid properties of Cu/SAPO-34 [16, 19–21].

Combining in situ diffuse reflectance infrared Fourier transform (DRIFT) reactions and characterization reveals the specific roles of the reaction sites in hydrothermal deactivation at low (150–400 °C) and high (400–550 °C) reaction temperatures. We hope that this discovery is useful in designing an NH_3-SCR catalyst with excellent hydrothermal stability over the entire reaction temperature range (150–550 °C).

2 Experimental

2.1 Preparation and hydrothermal aging of catalysts

The redox and acid properties were altered by changing the amount of PVA in the synthesis of SAPO-34. The molar composition of SAPO-34 gel is 1 Al_2O_3:1 P_2O_5:0.6 SiO_2:3.5 triethylamine (TEA):50 distilled water. Upon mixing pseudo-boehmite, H_3PO_4, and distilled H_2O, Gel A was formed. PVA (mass of 0.3, 1.0 and 1.5 g) was added to distill H_2O, followed by Si sols (analytical grade, AR, Shanghai Nalco, China) and TEA. This mixture was well-stirred as Solution B. Gel A was added to Solution B, forming a new solution. This well-mixed solution was allowed to stand at 25 °C for 12 h and then poured into a stainless, Teflon-lined autoclave. Hydrothermal crystallization was then conducted for 24 h at 200 °C. The solid product was washed three times with distilled H_2O and then dried completely at 105 °C. Finally, the product was treated for 6 h at 600 °C under flowing air. Copper nitrates were the precursors for preparing the Cu/SAPO-34 catalysts. All raw materials were AR reagents purchased from Chengdu Chron Chemicals (China) unless otherwise stated and used without further purification. The detailed methods are described in the section "Preparation of catalysts" in Supplementary Material.

A wash-coated catalytic monolith (Corning, USA) with approximately 120 $g{\cdot}L^{-1}$ was used for performance assessment. The prepared monolithic catalyst was age-accelerated at 700 °C for 10 h under flowing air containing 10 vol% H_2O. These samples were denoted as SA(X) and Cat(X)-F/HT (Table 1), where SA, Cat, and X represent Cu-free SAPO-34 zeolite, Cu/SAPO-34 catalyst, and the mass of PVA, respectively; F and HT represent fresh and hydrothermally aged catalysts, respectively. After hydrothermal aging, the catalysts exhibited hydrothermal deactivation, except Cat(0) without PVA. The performance deterioration at 150–400 and 400–550 °C is described as hydrothermal deactivation in the low- and high-reaction regions, respectively.

2.2 Physical and chemical characterization

X-ray photoelectron spectroscopy (XPS) was used to detect the surface concentrations and inductively coupled plasma-atomic emission spectrometry (ICP-AES, IRIS Advantage,

Table 1 Amounts of PVA and descriptions of samples

Amounts of PVA/g	Labels		Descriptions
	Zeolites	Catalysts	
0	SA(0)	Cat(0)	No performance deterioration
0.3	SA(0.3)	Cat(0.3)	Deactivation over entire temperature (150–550 °C) region
1.0	SA(1.0)	Cat(1.0)	Deactivation in high-temperature (400–550 °C) region
1.5	SA(1.5)	Cat(1.5)	Deactivation in low-temperature (150–400 °C) region

USA) revealed the Cu content, as shown in Table 2. The in situ DRIFT spectroscopy using a Nicolet 6700 (Thermo Fisher Scientific, USA) was conducted to study the possible mechanisms in the deactivation regions. The temperature-programmed reduction of hydrogen (H_2-TPR) and XPS was conducted to characterize the copper species, and the temperature-programmed desorption of NH_3 (NH_3-TPD) was performed to determine the acid sites. The structural properties were investigated using N_2 physisorption, X-ray diffraction (XRD), scanning electron microscopy (SEM), DRIFT spectroscopy, and ^{27}Al solid-state nuclear magnetic resonance (NMR) spectroscopy. The detailed experimental procedures and parameters are listed in the section "Characterization" in Supplementary Material.

2.3 Catalytic activity

The as-prepared monolithic catalysts were evaluated in NH_3-SCR from 150 to 550 °C. Before the study, pretreatment was performed under the mixed reactant gas balanced using N_2 with a total gaseous hourly space velocity of 40,000 h^{-1}. The pretreatment time and temperature were 1 h and 550 °C, respectively, and the mixed gas contained 220×10^{-6} NH_3, 200×10^{-6} NO, 10 vol% O_2, and 5 vol% H_2O. Using the gas concentrations monitored with gas Fourier transform infrared spectroscopy (FTIR, Nicolet Antaris IGS-6700, Thermo Fisher Scientific), the NO_x conversion is obtained at intervals of 50 °C using the following equation:

$$\text{NO conversion} = \left(1 - \frac{[\text{NO}]_{\text{out}} + [\text{NO}_2]_{\text{out}} + 2[\text{N}_2\text{O}]_{\text{out}}}{[\text{NO}_x]_{\text{in}}}\right) \times 100\% \quad (1)$$

where $[NO]_{out}$, $[NO_2]_{out}$, and $[N_2O]_{out}$ are the outlet concentrations ($\times 10^{-6}$) of NO, NO_2, and N_2O, respectively; $[NO_x]_{in}$ represents the total concentration (10^{-6}) of nitrogen oxides within the reactor.

Table 2 Molar ratios of Si/(Al + P) and Cu contents

Catalysts	Molar ratios of Si/(Al + P) [a]	Cu contents/wt%[b]
Cat(0)-F	0.03	3.43
Cat(0)-HT	0.03	3.36
Cat(0.3)-F	0.03	3.47
Cat(0.3)-HT	0.04	3.50
Cat(1.0)-F	0.03	3.41
Cat(1.0)-HT	0.03	3.37
Cat(1.5)-F	0.03	3.46
Cat(1.5)-HT	0.03	3.48

[a] Calculated based on XPS

[b] Acquired based on ICP-AES

3 Results and discussion

3.1 Properties of PVA-modified and unmodified samples

XRD patterns and morphologies of all Cu-free zeolites (Fig. 1a) reveal diffraction peaks and cubic phases that correspond to those of SAPO-34. Figure 1b and inset show the ^{27}Al solid-state NMR spectra and the integrated signal areas of the signals representing the framework tetra-coordinated Al (Al^{IV}) atoms, respectively. The water-soluble PVA at a low concentration (0.3 g) uniformly disperses into the zeolite precursors in the form of random coils, which are independent of each other because of extremely weak interactions [22]. The PVA coils enter the pores and channels, adsorbing on the surface of AlPO, assisting in the formation of pores and channels on SA(0.3), which yields a large Brunauer–Emmett–Teller surface area (S_{BET}) of 856 $m^2 \cdot g^{-1}$ (Table 3). In addition, PVA prevents the aggregation of the SiO_2 sols via hydrogen bonding. Overall, 0.3 g PVA improves the crystallinity of SAPO-34 and increases the content of framework Al^{IV} atoms by 11.6% [23]. The interaction strengthens with PVA concentration increasing, inducing the formation of three-dimensional (3D) networks that may fix precursors [21, 22, 24]. For an intermediate concentration of PVA (1.0 g), the 3D network and coils are

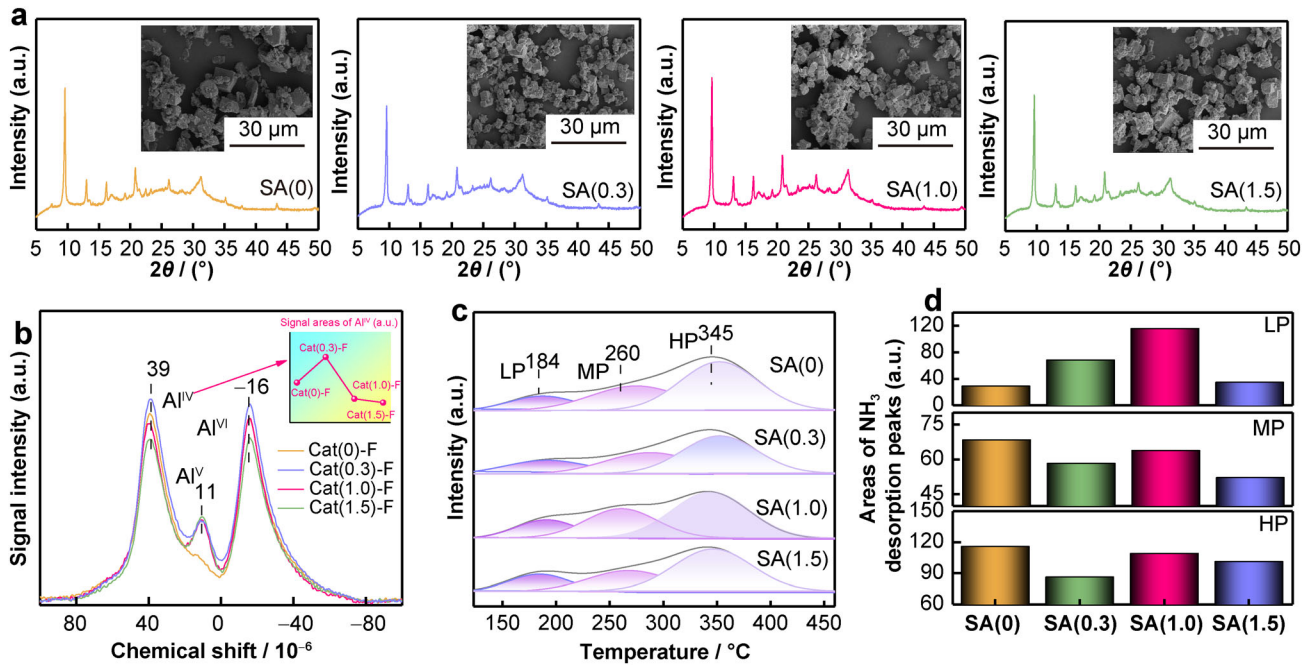

Fig. 1 **a** XRD patterns and (insets) SEM images of zeolites; **b** ^{27}Al solid-state NMR spectra and signal areas of Al^{IV} of Cat(0)-F, Cat(0.3)-F, Cat(1.0)-F, and Cat(1.5)-F; **c** NH_3-TPD profiles of zeolites; **d** quantified areas of NH_3-TPD

Table 3 Texture properties of zeolite

Zeolites	S_{BET}/($m^2 \cdot g^{-1}$)	T-plot micropore volumes/ ($cm^3 \cdot g^{-1}$)
SA(0)	530	0.19
SA(0.3)	856	0.31
SA(1.0)	839	0.30
SA(1.5)	524	0.19

observed, decreasing the content of Al^{IV} by 7.3%. In addition, the network fixes the crystal nucleus akin to the colloidal stabilizer, inhibiting the attachment of the precursors to the crystals [25, 26]. Thus, small and uniform crystals with sizes of 2–3 μm are formed on SA(1.0), which are smaller than the crystals of 6–7 μm on SA(0).

When the concentration of PVA is increased to 1.5 g, PVA mainly forms a large network. SAPO-34 exhibits a microporous structure, with pore sizes of generally < 2 nm. Thus, it is challenging for the large PVA network to enter the channels and pores of the SAPO-34 zeolite, resulting in less influence on the internal channels and pores. This is consistent with the similar textural properties of SA(0) and SA(1.5) (Table 3). Moreover, SA(1.5) consists of 4–6 μm crystals, which are also similar to those of 6–7 μm on SA(0). However, the barrier of the PVA network prevents the reaction between the silicate ions and AlPO, decreasing the content of Al^{IV} by 9.1%. The NH_3 desorption and quantified areas shown in Fig. 1c, d demonstrate that the unmodified SA(0) exhibits the largest moderate- (MP) and high-temperature peaks (HP) at 260 and 345 °C, which are ascribed to moderate and strong acid sites [27], respectively. The SA(1.0) zeolite shows the largest low-temperature peak (LP) at 186 °C, which is assigned to weak acid sites [28].

Therefore, different amounts of PVA successfully alter the properties of the SAPO-34 zeolites, which should further affect the reaction sites on the subsequently prepared Cu/SAPO-34 catalysts, with various hydrothermal durabilities at a high temperature (700 °C).

3.2 NH_3-SCR performance

Cu/SAPO-34 catalysts were prepared by the incipient wetness impregnation method using the prepared SAPO-34. The catalytic performance was then evaluated in triplicate, and the data with confidence intervals are shown in Fig. 2. Four types of hydrothermal deactivation in the reaction regions are successfully detected. The NH_3-SCR performance is retained on Cat(0)-HT. The NO_x conversion on Cat(0.3)-HT declines by > 7% in the low-reaction (150–400 °C) region and by > 10% in the high-reaction (400–550 °C) region. The hydrothermal deactivation of Cat(1.0)-HT is observed in the high-reaction region, with NO_x conversion decreasing by > 10%. The hydrothermal deactivation of Cat(1.5)-HT is observed in the low-reaction region, with the maximum loss of NO_x conversion reaching 6%. The amount of N_2O obtained as the by-product

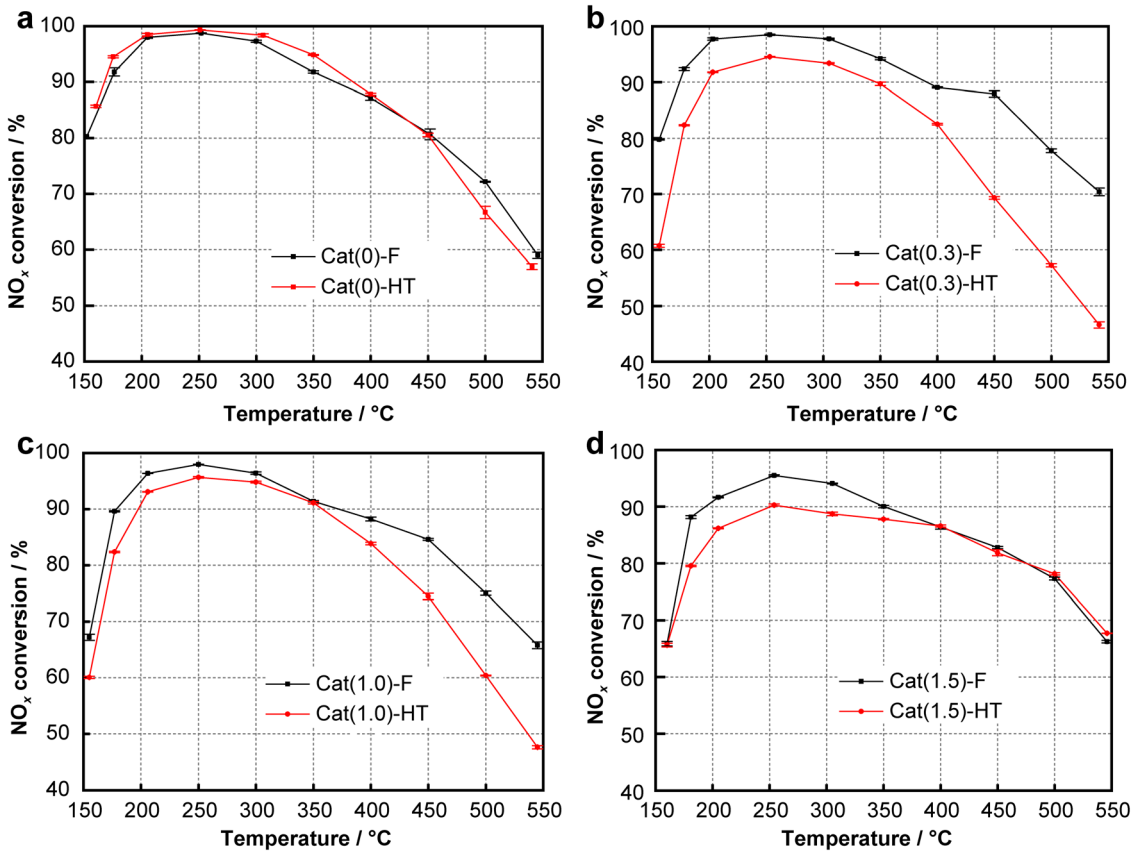

Fig. 2 NH_3-SCR performances of **a** Cat(0)-F/HT, **b** Cat(0.3)-F/HT, **c** Cat(1.0)-F/HT, and **d** Cat(1.5)-F/HT

(Fig. S1) is $< 7 \times 10^{-6}$, with no changes even after hydrothermal aging.

3.3 Possible reaction mechanisms in hydrothermal deactivation region

The surface molar ratios of Si/(Al + P) on fresh and hydrothermally aged catalysts are 0.03, with Cu contents also unchanged after hydrothermal aging (Table 2). Therefore, the hydrothermal deactivation is unrelated to the elemental compositions. In situ DRIFT reaction analysis of the pre-adsorbed species and gaseous reactants was conducted to investigate the possible reaction pathways in the hydrothermal deactivation region. NO_x conversion on Cat(0.3)-HT declines by ~ 7% at 200 °C and 11% at 450 °C, and therefore, Cat(0.3)-F/HT was used as representative examples. Furthermore, 200 and 450 °C were used as the evaluation temperatures. The in situ DRIFT reactions on Cat(0.3)-F/HT are shown in Fig. 3, and the results of the other catalysts are shown in Figs. S2–S4. The top panel of Fig. 3 shows that after Cat(0.3)-F/HT saturation with NH_3 gas at 200 °C, bands attributed to NH_4^+ species adsorbed at Brønsted acid sites (BAS) are observed at ~ 1463, 1717, 3278, and 3369 cm^{-1} [29–31]. Further, bands at ~ 1614 and 3187 cm^{-1} are assigned to NH_3 species coordinated at Lewis acid sites (LAS) [32–34]. The bands decrease while introducing NO + O_2 into the saturated catalyst by NH_3, suggesting the participation of the absorbed ammonia species in the catalytic reaction. The band at ~ 1614 cm^{-1} related to Cu^{2+} is attributed to NH_3 species initially and then nitrate at ~ 1618 cm^{-1} as the reaction proceeds [35].

While introducing the mixture of NO and O_2 at 200 °C, only a band at 1622 cm^{-1} is attributed to the bridged nitrate generated at the substituted Cu sites [36, 37]. After nitrate consumption by NH_3, adsorbed ammonia species accumulate again on the surface. Adsorbed ammonia species and bridged nitrate cooperate in the catalytic reaction at 200 °C, corresponding to the L–H mechanism. Additionally, no adsorbed nitrate at 450 °C induces the E–R mechanism, where adsorbed ammonia species are the critical active intermediates. After hydrothermal aging, the same adsorbed species are observed over Cat(0.3)-F/HT, demonstrating the unchanged mechanism in the hydrothermal deactivation regions. The trend observed over the other catalysts also verifies this view (Figs. S2–S4). Besides, the rate and apparent activation energy (E_a)

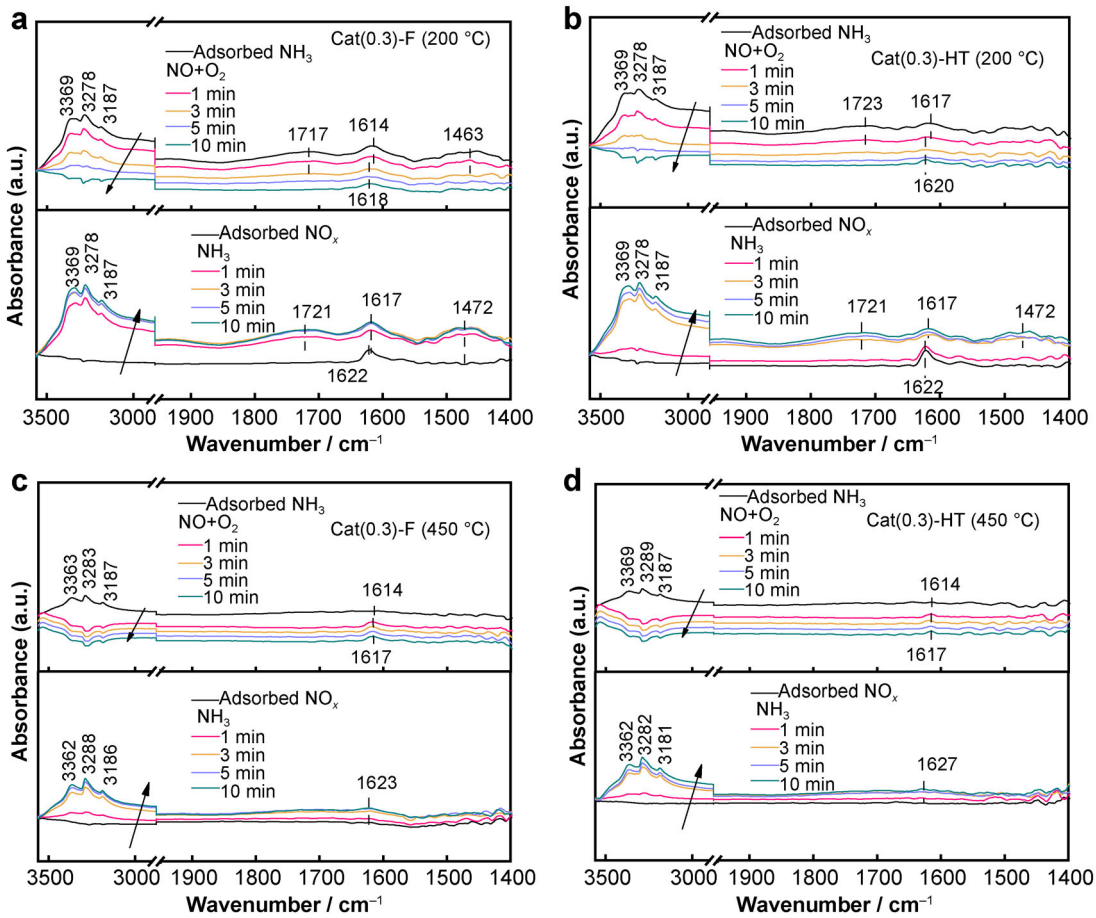

Fig. 3 In situ DRIFT reactions between pre-adsorbed species and gaseous reactants on **a** Cat(0.3)-F (200 °C), **b** Cat(0.3)-HT (200 °C), **c** Cat(0.3)-F (450 °C) and **d** Cat(0.3)-HT (450 °C) at 1, 3, 5 or 10 min (top part of every panel representing spectra exposed to NH_3 followed by NO + O_2 for various time; bottom part representing spectra exposed to NO + O_2 followed by NH_3 for various time)

were calculated according to the formulas in Supplementary Material. E_a before and after hydrothermal aging is calculated based on the kinetic data, as shown in Fig. S5. Because E_a is related to active species, the similar values confirm the unchanged mechanism after hydrothermal aging [38].

3.4 Hydrothermal deactivation in low-reaction (150–400 °C) region

3.4.1 Redox sites

The performance deteriorations on Cat(0.3)-HT and Cat(1.5)-HT are centered in the low-reaction (150–400 °C) region. The isolated Cu^{2+} and surface oxygen species participate in the redox cycle of the NH_3-SCR reaction. Figure 4a depicts the results of H_2-TPR. Cat(0.3)-HT and Cat(1.5)-HT exhibit decreases in isolated Cu^{2+} by 7.1 and 13.6 μmol·g^{-1}, respectively. This is consistent with the changed Region I observed in the ultraviolet–visible spectra (Fig. S6a).

Figure 4b shows O 1s regions in the XPS profiles, with peaks attributed to surface chemisorbed oxygen O_β (denoted as $O_{\beta1}$ and $O_{\beta2}$ at 533.1 and 534.9 eV, respectively), and lattice oxygen O^{2-} (denoted as O_α at 531.7 eV) [30, 39]. The $O_{\beta1}$ species include O^-, O_2^{2-} and O_2^- [40, 41], and $O_{\beta2}$ represents the oxygen within the hydroxyl groups of Si–OH–Al or oxide defects [42, 43]. O_β species easily transfer electrons between the surface adsorbed dioxygen and the gaseous oxygen, exhibiting higher mobility than O_α species [44]. Herein, O_β species are generally the critical oxygen species for oxidizing NO, greatly contributing to the catalytic efficiency via the "fast NH_3-SCR" reaction [42]. As listed in Table 4, the percentage of O_β in total O species (O_β/O_{tol}) decrease from 0.53 on Cat(0.3)-F to 0.49 on Cat(0.3)-HT and 0.51 on Cat(1.5)-F to 0.49 on Cat(1.5)-HT. In addition, the surface chemisorbed oxygen species weaken the negative influence of the 0.41 wt% decrease in the surface isolated Cu^{2+} from Cat(1.0)-F to Cat(1.0)-HT (Table 4 and Fig. S6a) [44, 45].

Thus, isolated Cu^{2+} and O_β species collectively determine the hydrothermal deactivation in the low-reaction

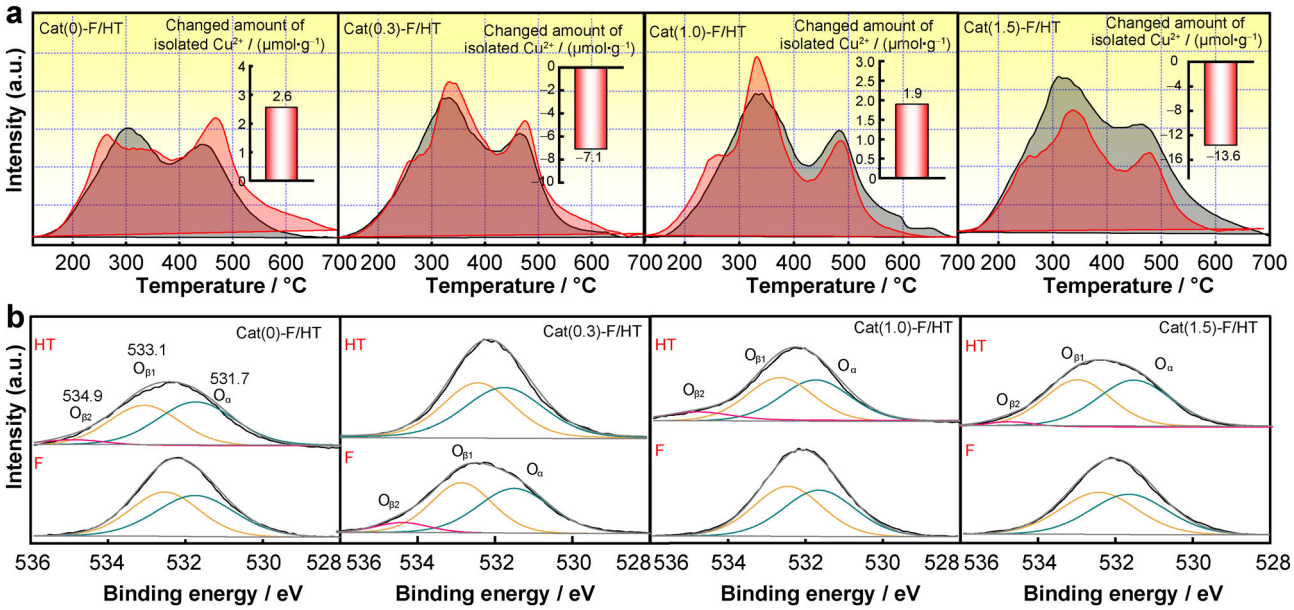

Fig. 4 **a** H_2-TPR (gray and red curves representing F and HT catalysts, respectively) and change in isolated Cu^{2+} and **b** O 1s XPS profiles of Cat(0)-F/HT, Cat(0.3)-F/HT, Cat(1.0)-F/HT and Cat(1.5)-F/HT

Table 4 Concentrations of surface species and textural properties

Catalysts	Isolated Cu^{2+}/wt%	O_β/O_{tol}	Al_β/wt%	$S_{BET}/(m^2 \cdot g^{-1})$	T-plot micropore volumes/$(cm^3 \cdot g^{-1})$
Cat(0)-F	1.15	0.48	3.66	334	0.12
Cat(0)-HT	1.03	0.49	4.33	302 (9.6%)*	0.10
Cat(0.3)-F	1.40	0.53	1.95	577	0.20
Cat(0.3)-HT	1.24	0.49	3.00	325 (43.7%)*	0.11
Cat(1.0)-F	1.65	0.51	3.49	366	0.13
Cat(1.0)-HT	1.24	0.54	5.81	296 (19.1%)*	0.10
Cat(1.5)-F	1.20	0.51	5.14	484	0.16
Cat(1.5)-HT	0.88	0.49	2.06	454 (6.2%)*	0.17

*Decline in S_{BET} after hydrothermal aging

(150–400 °C) region. The bridged nitrates are involved in the catalytic reaction in this region based on the L–H mechanism, with the NO_x emission control ($deNO_x$) easily affected by the redox sites (the isolated Cu^{2+} and surface chemisorbed oxygen).

3.4.2 Acid sites

The alkaline NH_3 molecules probe the acid sites. The NH_3 desorption profiles, as shown in Fig. 5a, are well-fitted into three regions (LP, MP, and HP). As demonstrated by the integrated areas (Fig. 5b), LP on Cat(0.3)-HT decreases by ~ 23.2%, showing a severe performance deterioration in the low-reaction (150–400 °C) region. Furthermore, Cat(1.5)-HT also exhibits a severe deactivation in this region, with an LP loss of 5.7%. Generally, LP is attributed to weak acid sites [46], and thus, the loss of weak acid sites accelerates the performance deterioration in this region.

3.5 Hydrothermal deactivation in high-reaction (400–550 °C) region

The performances of Cat(0.3)-HT and Cat(1.0)-HT deteriorate in the high-reaction (400–550 °C) region. However, Cat(1.0)-HT still bears the newly generated redox sites (Fig. 4). In addition, the NH_3 oxidation conversion and product distribution (upper-left and lower-right insets in Fig. S7, respectively) suggest no aggravated NH_3 oxidation after hydrothermal aging. Hence, the redox sites (copper species and O_β) are independent of the performance deterioration in this region [47–49].

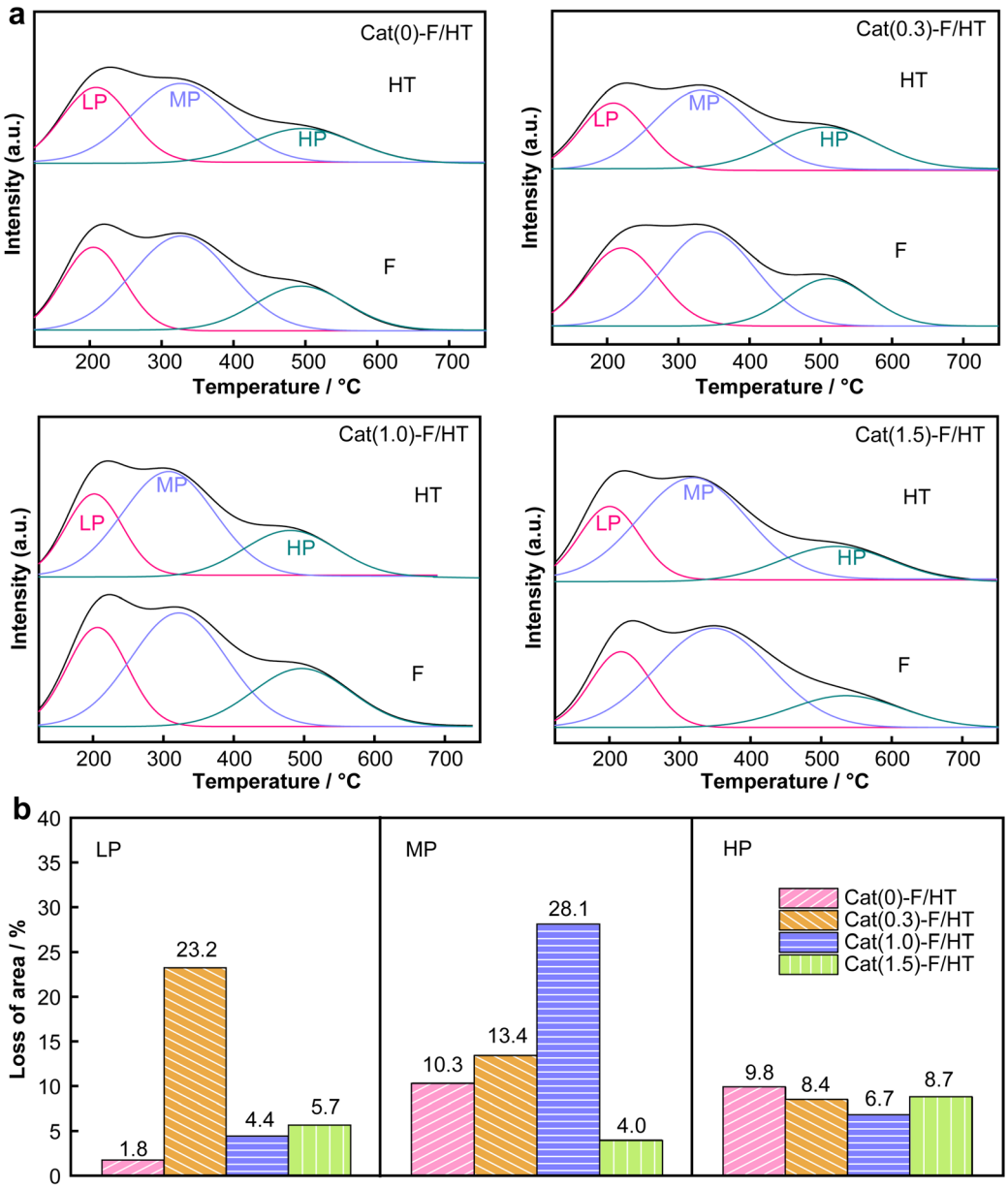

Fig. 5 **a** NH_3-TPD and **b** decline in acid sites after hydrothermal aging of Cat(0)-F/HT, Cat(0.3)-F/HT, Cat(1.0)-F/HT and Cat(1.5)-F/HT

3.5.1 Acid sites

The declines in MP are 13.4% and 28.1% on Cat(0.3)-HT and Cat(1.0)-HT, respectively. Moreover, both catalysts exhibit considerable decreases in HP by 8.4% and 6.7%, respectively. Generally, MP and HP are regarded as strong LAS and strong BAS associated with the zeolite framework, respectively [49, 50]. The in situ DRIFT reactions, as shown in Fig. 3, also confirm the presence of LAS and BAS in the high-reaction (400–550 °C) region. Therefore, both acid sites determine the hydrothermal deactivation in this region.

3.5.2 Relationship between structural stability and acid sites

The decreased diffraction peak (Fig. S8) is generally related to the collapse of the structure [51–53]. According to the peak intensity at $2\theta = 9.5°$, Cat(0)-HT and Cat(1.5)-HT show 5% and 10% loss, respectively, which are much lesser than that observed over Cat(0.3)-HT (20%) and Cat(1.0)-HT (19%), as shown in Fig. 6a. In addition, the textural properties (Table 4) show that S_{BET} decreases by 9.6% and 6.2% on Cat(0)-HT and Cat(1.5)-HT, respectively, which are also much lower than those on Cat(0.3)-

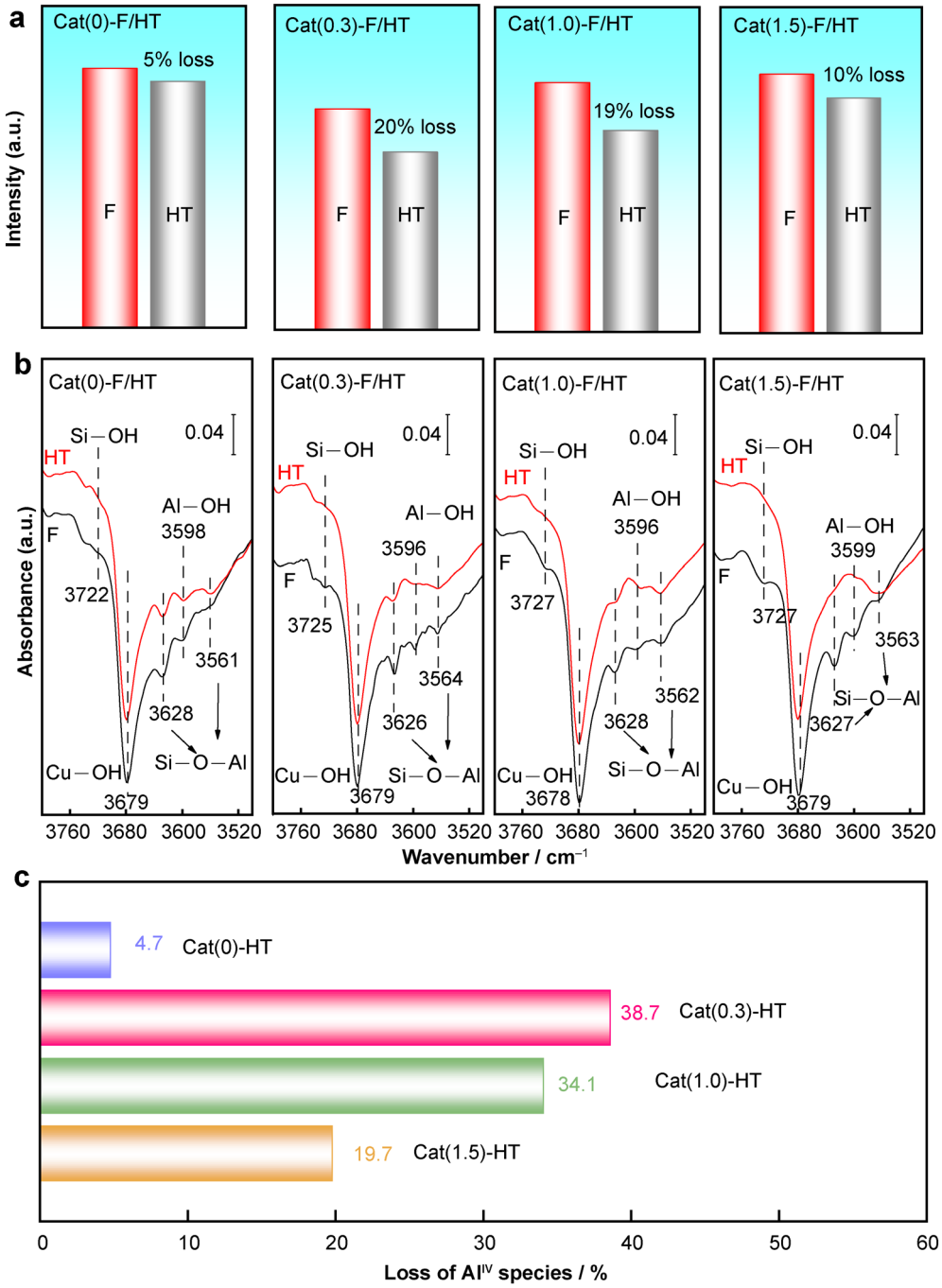

Fig. 6 **a** Intensities and losses of main diffraction peaks, **b** DRIFT spectra of OH vibrational regions after NH_3 adsorption at 50 °C, and **c** lost Al^{IV} species after hydrothermal aging based on ^{27}Al solid-state NMR spectroscopy of Cat(0)-F/HT, Cat(0.3)-F/HT, Cat(1.0)-F/HT and Cat(1.5)-F/HT

HT (43.7%) and Cat(1.0)-HT (19.1%). The diffraction intensity and S_{BET} reveal the poor structural stabilities of Cat(0.3)-HT and Cat(1.0)-HT, which is consistent with the changes in their morphologies, as shown in Fig. S9. The cleavage of the framework Si(OAl) structures results in the structural collapse of Cu/SAPO-34. As shown in Fig. 6b, bands at 3628 and 3561 cm^{-1} represent the stretching vibrations of Si(OAl) structures located in the eight-member and double six-member rings, respectively [54–57]. Few changes in the intensities in the spectra of Cat(0)-HT and Cat(1.5)-HT suggest that most Si(OAl) remains intact, consistent with their stable structures. The signals representing the Si(OAl) structures clearly deteriorate in the DRIFT spectra of Cat(0.3)-HT and Cat(1.0)-

HT, also demonstrating their poor structural stabilities. ^{27}Al solid-state NMR spectroscopy (Fig. S10) is a powerful tool for analyzing the framework Al^{IV} atoms. The loss results (Fig. 6c) show that Al^{IV} species decrease by 4.7%, 19.7%, 38.7%, and 34.1% on Cat(0)-HT, Cat(1.5)-HT, Cat(0.3)-HT, and Cat(1.0)-HT, respectively. The two former samples lose lower concentrations of Al^{IV}, with the Si(OAl) structures undergoing attenuated hydrolysis during hydrothermal aging. The weaker hydrolysis is consistent with the superior structural integrities of Cat(0)-HT and Cat(1.5)-HT compared to those of Cat(0.3)-HT and Cat(1.0)-HT.

The framework Si(OAl) structures deteriorate to extra-framework Al_β species [58]. As demonstrated by the results listed in Table 4 based on the Al 2p XPS profiles (Fig. S11), the Al_β species on Cat(0.3)-HT and Cat(1.0)-HT increase by 1.1 wt% and 2.3 wt%, respectively, which are clearly higher than those (0.7 wt% and –3.1 wt%) on Cat(0)-HT and Cat(1.5)-HT, respectively. Thus, the structural stability is closely related to the strong LAS/BAS, accelerating the performance deterioration in the high-reaction (400–550 °C) region.

4 Conclusion

This work investigated the critical roles of various reaction sites on hydrothermal deactivation in the low- (150–400 °C) and high-reaction (400–550 °C) regions over Cu/SAPO-34. First, the hydrothermal deactivation in these two regions was successfully manipulated over Cu/SAPO-34 using PVA. Then, the deactivation region was analyzed in terms of the detailed roles of the redox/acid sites. The results verified that the catalytic reactions at the low (150–400 °C) and high (400–550 °C) reaction temperatures still predominantly follow the L–H and E–R mechanisms, respectively, even after hydrothermal deactivation. However, the key difference on the reactant sites results in "seagull"-shaped NO_x conversion profiles over Cu/SAPO-34 after hydrothermal aging, with an inflection point at 400 °C. The low-reaction region requires adsorbed nitrates/ammonia species, and therefore, hydrothermal deactivation in this region can be suppressed by optimizing the easily reducible isolated Cu^{2+}, surface chemical oxygen, and weak acid sites. The adsorbed/activated ammonia species dominate in the high-reaction region, with restrained performance deterioration due to the increased stability of the moderate/strong acid sites related to the structure. This work provides several theoretical insights to optimize the hydrothermal stabilities of the Cu/zeolite catalysts.

Acknowledgements This study was financially supported by the National Natural Science Foundation of China (Nos. 22072098 and 21802099), Sichuan Science and Technology Program (No. 2021YJ0333) and the National Engineering Laboratory for Mobile Source Emission Control Technology (No. NELMS2017A06).

Declarations

Conflict of interests The authors declare that they have no conflict of interest.

References

[1] Han L, Cai S, Gao M, Hasegawa JY, Wang P, Zhang J, Shi L, Zhang D. Selective catalytic reduction of NO_x with NH_3 by using novel catalysts: state of the art and future prospects. Chem Rev. 2019;119(19):10916.
[2] Zhang Y, Peng Y, Li K, Liu S, Chen J, Li J, Gao F, Peden CHF. Using transient FTIR spectroscopy to probe active sites and reaction intermediates for selective catalytic reduction of NO on Cu/SSZ-13 catalysts. ACS Catal. 2019;9(7):6137.
[3] Su W, Chang H, Peng Y, Zhang C, Li J. Reaction pathway investigation on the selective catalytic reduction of NO with NH_3 over Cu/SSZ-13 at low temperatures. Environ Sci Technol. 2015;49(1):467.
[4] Zhang T, Qiu F, Chang H, Li X, Li J. Identification of active sites and reaction mechanism on low-temperature SCR activity over Cu-SSZ-13 catalysts prepared by different methods. Catal Sci Technol. 2016;6(16):6294.
[5] Liu J, Zhao Z, Xu C, Liu J. Structure, synthesis, and catalytic properties of nanosize cerium-zirconium-based solid solutions in environmental catalysis. Chin J Catal. 2019;40(10):1438.
[6] Borfecchia E, Beato P, Svelle S, Olsbye U, Lamberti C, Bordiga S. Cu-CHA-a model system for applied selective redox catalysis. Chem Soc Rev. 2018;47(22):8097.
[7] Shao X, Wang H, Yuan M, Yang J, Zhan W, Wang L, Guo Y, Lu G. Thermal stability of Si-doped V_2O_5/WO_3–TiO_2 for selective catalytic reduction of NO_x by NH_3. Rare Met. 2019;38(4):292.
[8] Zhang N, Li L, Guo Y, He J, Wu R, Song L, Zhang G, Zhao J, Wang D, He H. A MnO_2-based catalyst with H_2O resistance for NH_3-SCR: study of catalytic activity and reactants-H_2O competitive adsorption. Appl Catal B. 2020;270:118860.
[9] Xu S, Lin Q, Liu S, Lin J, Xu H, Wang J, Chen Y. Promotional effects of silanization on the hydrothermal stability of CuCe/BEA catalyst for selective catalytic reduction of NO_x with NH_3. Chin J Inorg Chem. 2020;36(12):2385.
[10] Lin Q, Liu S, Xu S, Liu J, Xu H, Chen Y, Dan Y. Fabricate surface structure-stabilized Cu/BEA with hydrothermal-resistant via Si-deposition for NO_x abatement. Mol Catal. 2020;495:111153.
[11] Feng X, Cao Y, Lan L, Lin C, Li Y, Xu H, Gong M, Chen Y. The promotional effect of Ce on CuFe/beta monolith catalyst for selective catalytic reduction of NO_x by ammonia. Chem Eng J. 2016;302:697.
[12] Fan C, Chen Z, Pang L, Ming S, Dong C, Brou Albert K, Liu P, Wang J, Zhu D, Chen H, Li T. Steam and alkali resistant Cu-SSZ-13 catalyst for the selective catalytic reduction of NO_x in diesel exhaust. Chem Eng J. 2018;334:344.
[13] Fan D, Wang J, Yu T, Wang J, Hu X, Shen M. Catalytic deactivation mechanism research over Cu/SAPO-34 catalysts for NH_3-SCR (I): the impact of 950 °C hydrothermal aging time. Chem Eng Sci. 2018;176:285.
[14] Leistner K, Kumar A, Kamasamudram K, Olsson L. Mechanistic study of hydrothermally aged Cu/SSZ-13 catalysts for ammonia-SCR. Catal Today. 2018;307:55.

[15] Tan J, Liu Z, He C, Liu X, Han X, Zhai R, Bao X. Study on the crystallization mechanism of molecular sieve SAPO-34. Chin J Catal. 1998;19(5):436.
[16] Yin X, Chu N, Lu X, Li Z, Guo H. Studies on the formation of hierarchical zeolite T aggregates with well-defined morphology in different template systems. Solid State Sci. 2016;51:30.
[17] Chen Y, Rao W, Zhou R. Influence of surfactant (PVA) concentration on the preparation of copper nanoparticles by using electron beam-irradiation method. Chem Eng. 2007;12:4.
[18] Xing A, Feng Q, Zhang X, Jian J. Development in crystallization mechanism and crystallization kinetics of SAPO-34 molecular sieves. Ind Catal. 2016;24(2):5.
[19] Li Y, Han X, Hou Y, Guo Y, Liu Y, Cui Y, Huang Z. Role of CTAB in the improved H_2O resistance for selective catalytic reduction of NO with NH_3 over iron titanium catalyst. Chem Eng J. 2018;347:313.
[20] Li R, Wang P, Ma S, Yuan F, Li Z, Zhu Y. Excellent selective catalytic reduction of NO_x by NH_3 over Cu/SAPO-34 with hierarchical pore structure. Chem Eng J. 2020;379:122376.
[21] Du Q, Guo Y, Duan H, Li H, Chen Y, Liu H. Synthesis of hierarchical TS-1 zeolite via a novel three-step crystallization method and its excellent catalytic performance in oxidative desulfurization. Fuel. 2017;188:232.
[22] Du Q, Guo Y, Wu P, Liu H. Synthesis of hierarchically porous TS-1 zeolite with excellent deep desulfurization performance under mild conditions. Micropor Mesopor Mater. 2018;264:272.
[23] Paul G, Bisio C, Braschi I, Cossi M, Gatti G, Gianotti E, Marchese L. Combined solid-state NMR, FT-IR and computational studies on layered and porous materials. Chem Soc Rev. 2018;47(15):5684.
[24] Zhou M, Liu X, Zhang B, Zhu H. Assembly of oriented zeolite monolayers and thin films on polymeric surfaces via hydrogen bonding. Langmuir. 2008;24:11942.
[25] Liu J, Luo Y, Li M, Shu X. Synthesis of nanosized SSZ-13 zeolite and performance of its mixed matrix membrane for CO_2/CH_4 separation. China Pet Process Pe. 2019;21(2):19.
[26] Kumar M, Luo H, Román-Leshkov Y, Rimer JD. SSZ-13 crystallization by particle attachment and deterministic pathways to crystal size control. J Am Chem Soc. 2015;137(40):13007.
[27] Wang C, Xu Q, Wang L, Zhan W, Guo Y, Guo Y. Effect of metal modification on NH_3-SCR reaction performance of Cu-SAPO-34 catalyst. Chin J Rare Met. 2020;44(2):159.
[28] Han M, Jiao Y, Zhou C, Guo Y, Guo Y, Lu G, Wang L, Zhan W. Catalytic activity of Cu-SSZ-13 prepared with different methods for NH_3-SCR reaction. Rare Met. 2019;38(3):210.
[29] Chen P, Moos R, Simon U. Metal loading affects the proton transport properties and the reaction monitoring performance of Fe-ZSM-5 and Cu-ZSM-5 in NH_3-SCR. J Phy Chem C. 2016;120(44):25361.
[30] Fan J, Ning P, Wang Y, Song Z, Liu X, Wang H, Wang J, Wang L, Zhang Q. Significant promoting effect of Ce or La on the hydrothermal stability of Cu-SAPO-34 catalyst for NH_3-SCR reaction. Chem Eng J. 2019;369:908.
[31] Zhang J, Liu F, Liang J, Yu H, Liu W, Wang X, Peng H, Wu P. Exploring the nanosize effect of mordenite zeolites on their performance in the removal of NO_x. Ind Eng Chem Res. 2019;58:8625.
[32] Ma L, Cheng Y, Cavataio G, McCabe RW, Fu L, Li J. In situ DRIFTS and temperature-programmed technology study on NH_3-SCR of NO_x over Cu-SSZ-13 and Cu-SAPO-34 catalysts. Appl Catal B. 2014;156–157:428.
[33] Chen P, Rauch D, Weide P, Schönebaum S, Simons T, Muhler M, Moos R, Simon U. The effect of Cu and Fe cations on NH_3-supported proton transport in DeNO_x-SCR zeolite catalysts. Catal Sci Technol. 2016;6(10):3362.
[34] Cao Y, Fan D, Sun L, Yang M, Cao L, Sun T, Xu S, Tian P, Liu Z. The self-protection effect of reactant gas on the moisture stability of CuSAPO-34 catalyst for NH_3-SCR. Chem Eng J. 2019;374:832.
[35] Lezcano-Gonzalez I, Deka U, Arstad B, Van Yperen-De DA, Hemelsoet K, Waroquier M, Van Speybroec V, Weckhuysen BM, Beale AM. Determining the storage, availability and reactivity of NH_3 within Cu-Chabazite-based ammonia selective catalytic reduction systems. Phys Chem Chem Phys. 2014;16(4):1639.
[36] Ryu T, Kim H, Hong SB. Nature of active sites in Cu-LTA NH_3-SCR catalysts: a comparative study with Cu-SSZ-13. Appl Catal B. 2019;245:513.
[37] Jiang H, Guan B, Peng X, Zhan R, Lin H, Huang Z. Influence of synthesis method on catalytic properties and hydrothermal stability of Cu/SSZ-13 for NH_3-SCR reaction. Chem Eng J. 2020;379:122358.
[38] Ming S, Chen Z, Fan C, Pang L, Guo W, Albert KB, Liu P, Li T. The effect of copper loading and silicon content on catalytic activity and hydrothermal stability of Cu-SAPO-18 catalyst for NH_3-SCR. Appl Catal A. 2018;599:47.
[39] Yu C, Huang B, Dong L, Chen F, Yang Y, Fan Y, Yang Y, Liu X, Wang X. Effect of Pr/Ce addition on the catalytic performance and SO_2 resistance of highly dispersed MnO_x/SAPO-34 catalyst for NH_3-SCR at low temperature. Chem Eng J. 2017;316:1059.
[40] Deng W, Dai Q, Lao Y, Shi B, Wang X. Low temperature catalytic combustion of 1,2-dichlorobenzene over CeO_2-TiO_2 mixed oxide catalysts. Appl Catal B. 2016;181:848.
[41] Shi X, Chu B, Wang F, Wei X, Teng L, Fan M, Li B, Dong L, Dong L. Mn-modified CuO, $CuFe_2O_4$, and gamma-Fe_2O_3 Three-phase strong synergistic coexistence catalyst system for NO reduction by CO with a wider active window. ACS Appl Mater Interf. 2018;10(47):40509.
[42] Shi Y, Wang X, Chen L, Li S, Wu C, Shan S, Li W. In situ DRIFT study on NH_3 selective catalytic reduction of NO over HBEA zeolite doped with CeO_2. Appl Surf Sci. 2020;506:144715.
[43] Cheng J, Han S, Ye Q, Cheng S, Kang T, Dai H. Selective catalytic reduction of NO with NH_3 over the Cu/SAPO-34 catalysts derived from different Cu precursors. Micropor Mesopor Mater. 2019;278:423.
[44] Chen C, Cao Y, Liu S, Chen J, Jia W. The catalytic properties of Cu modified attapulgite in NH_3-SCO and NH_3-SCR reactions. Appl Surf Sci. 2019;480:537.
[45] Li G, Wang B, Wang H, Ma J, Xu WQ, Li Y, Han Y, Sun Q. Fe and/or Mn oxides supported on fly ash-derived SBA-15 for low-temperature NH_3-SCR. Catal Commun. 2018;108:82.
[46] Xu H, Lin C, Lin Q, Feng X, Zhang Z, Wang Y, Chen Y. Grain size effect on the high-temperature hydrothermal stability of Cu/SAPO-34 catalysts for NH_3-SCR. J Environ Chem Eng. 2020;8(6):104559.
[47] Wang C, Yan W, Wang Z, Chen Z, Wang J, Wang J, Wang J, Shen M, Kang X. The role of alkali metal ions on hydrothermal stability of Cu/SSZ-13 NH_3-SCR catalysts. Catal Today. 2020;355:482.
[48] Wang H, Xu R, Jin Y, Zhang R. Zeolite structure effects on Cu active center, SCR performance and stability of Cu-zeolite catalysts. Catal Today. 2019;327:295.
[49] Chang H, Qin X, Ma L, Zhang T, Li J. Cu/SAPO-34 prepared by a facile ball milling method for enhanced catalytic performance in the selective catalytic reduction of NO_x with NH_3. Phys Chem Chem Phys. 2019;21(39):22113.
[50] Yang G, Du X, Ran J, Wang X, Chen Y, Zhang L, Rac V, Rakic V, Crittenden J. Irregular influence of alkali metals on Cu-SAPO-34 catalyst for selective catalytic reduction of NO_x with ammonia. J Hazard Mater. 2020;387:122007.
[51] Su W, Li Z, Peng Y, Li J. Correlation of the changes in the framework and active Cu sites for typical Cu/CHA zeolites

(SSZ-13 and SAPO-34) during hydrothermal aging. Phys Chem Chem Phys. 2015;17(43):29142.
[52] Shan Y, Shan W, Shi X, Du J, Yu Y, He H. A comparative study of the activity and hydrothermal stability of Al-rich Cu-SSZ-39 and Cu-SSZ-13. Appl Catal B. 2020;264:118511.
[53] Wang A, Chen Y, Walter ED, Washton NM, Varga T, Wang Y, Szanyi J, Wang Y, Peden CHF, Gao F. Remarkable self-degradation of Cu/SAPO-34 selective catalytic reduction catalysts during storage at ambient conditions. Catal Today. 2021;360:367.
[54] Liu B, Yao D, Wu F, Wei L, Li X, Wang X. Experimental investigation on N_2O formation during the selective catalytic reduction of NO_x with NH_3 over Cu-SSZ-13. Ind Eng Chem Res. 2019;58(45):20516.
[55] Zhu N, Lian Z, Zhang Y, Shan W, He H. The promotional effect of H_2 reduction treatment on the low-temperature NH_3-SCR activity of Cu/SAPO-18. Appl Surf Sci. 2019;483:536.
[56] Bordiga S, Lamberti C, Bonino F, Travert A, Thibault-Starzyk F. Probing zeolites by vibrational spectroscopies. Chem Soc Rev. 2015;44(20):7262.
[57] Gao F, Washton NM, Wang Y, Kollár M, Szanyi J, Peden CHF. Effects of Si/Al ratio on Cu/SSZ-13 NH_3-SCR catalysts: implications for the active Cu species and the roles of Brønsted acidity. J Catal. 2015;331:25.
[58] Liu Q, Liu B, Liu Q, Xu R, Xia H. Lattice substitution and desulfurization kinetic analysis of Zn-based spinel sorbents loading onto porous silicoaluminophosphate zeolites. J Hazard Mater. 2020;383:121151.